

UNLIMITED DISTRIBUTION

①



AD-A221 962

National Defence
Research and
Development Branch

Défense nationale
Bureau de recherche
et développement

TECHNICAL MEMORANDUM 90/202

March 1990

NOISE FROM
TIP VORTEX AND BUBBLE CAVITATION

Neil C. Sponagle

DTIC
ELECTE
MAY 25 1990
S B D

**Defence
Research
Establishment
Atlantic**



**Centre de
Recherches pour la
Défense
Atlantique**

Canada

DISTRIBUTION STATEMENT A

Approved for public release;
Distribution Unlimited

90 95 24 006

DEFENCE RESEARCH ESTABLISHMENT ATLANTIC

9 GROVE STREET

P.O. BOX 1012
DARTMOUTH, N.S.
B2Y 3Z7

TELEPHONE
(902) 426-3100

CENTRE DE RECHERCHES POUR LA DÉFENSE ATLANTIQUE

9 GROVE STREET

C.P. 1012
DARTMOUTH, N.E.
B2Y 3Z7



National Defence
Research and
Development Branch

Défense nationale
Bureau de recherche
et développement

NOISE FROM
TIP VORTEX AND BUBBLE CAVITATION

Neil C. Sponagle

March 1990

Approved by L.J. Leggat
Director / Technology Division

Distribution Approved by

Acting Director / Technology Division

TECHNICAL MEMORANDUM 90/202

Defence
Research
Establishment
Atlantic



Centre de
Recherches pour la
Défense
Atlantique

Canada

Abstract

This paper presents results from experiments designed to study the sound from different types of propeller cavitation. The propellers used in the tests produced tip vortex and travelling bubble cavitation. The spectral content, directivity, and waveform of the far-field sound were measured, in essentially free-field conditions, up to 100 kHz. These data were then correlated with information about the cavity dynamics, obtained from visual observations. Vibrational modes on the tip vortex cavities produced sound at characteristic frequencies. Bubble cavitation by itself produced very broadband noise, and strongly affected the vortex cavitation noise mechanisms if the free bubbles entered the tip vortices. The noise from both kinds of cavitation was directional.

Résumé

Cet article présente les résultats d'expériences visant l'étude des sons produits par divers types de cavitation des hélices. Les hélices utilisées dans ces essais produisaient de la cavitation des tourbillons d'extrémité et des bulles progressives. On a mesuré les composantes spectrales, la directivité et la forme d'onde des sons dans le champ lointain en conditions correspondant essentiellement au champ libre, jusqu'à 100 kHz. Ces données ont ensuite été corrélées avec les données de dynamique des cavités, obtenues par observation visuelle. Les modes de vibration dans les cavités de tourbillons d'extrémité produisaient des sons à des fréquences caractéristiques. Quant à la cavitation des bulles, elle produisait du bruit en bande très large et influait fortement sur les mécanismes du bruit de cavitation des tourbillons lorsque des bulles libres pénétraient dans les tourbillons d'extrémité. Le bruit était directionnel pour les deux types de cavitation.

Contents

Abstract	ii
Notation	iv
1 Introduction	1
2 Experiment	1
2.1 Apparatus	2
2.2 Calibrations	3
2.3 Acoustic Environment	3
3 Propellers	5
4 Cavitation Noise Spectra	6
4.1 Propeller TV1	6
4.2 Propeller BB	7
4.3 Propeller TV2	7
5 Cavitation Noise Directivity	7
5.1 Propeller TV1	7
5.2 Propeller BB	8
6 Cavitation Noise Waveform Analysis	8
7 Discussion	10
7.1 Tip Vortex Cavitation	10
7.1.1 Low Intensity Modes	10
7.1.2 High Intensity Modes	11
7.2 Bubble Cavitation	11
7.3 Cavitation Noise Directivity	12
8 Concluding Remarks	12
Figures	14
References	33

Accession For	
NTIS GRA&I	<input checked="" type="checkbox"/>
DTIC TAB	<input type="checkbox"/>
Unannounced	<input type="checkbox"/>
Justification	
By	
Distribution/	
Availability Codes	
Dist	Avail and/or Special
A-1	

Notation

A_b	reflection coefficient of the barge reflection
A_s	reflection coefficient of the surface reflection
a	vortex radius
F_P	probability density of P
$F_{P'}$	probability density of P'
f	frequency
f_a	frequency of spectral peak a
f_b	frequency of spectral peak b
f_l	lower cutoff frequency
f_m	frequency of vortex mode m
f_u	upper cutoff frequency
k	acoustic wave number
M	Mach number
m	vortex mode number
N	normal probability density
P	acoustic pressure
P'	acoustic pressure normalized as in Equation 5
P_f	free-field acoustic pressure
p_0	static pressure
p_v	vapour pressure
r_b	length of barge reflection path
r_d	length of direct path
r_s	length of surface reflection path
S	spectral density
S_f	free-field spectral density
s	standard deviation
t	time
u_θ	vortex surface speed
x	position coordinate
y	position coordinate
z	position coordinate
θ	angle from downstream propeller axis
θ_d	angle of propeller drive motor
μ	viscosity
ρ	density
τ_b	propagation time along the barge reflection path
τ_d	propagation time along the direct path
τ_s	propagation time along the surface reflection path
ω	angular frequency

1 Introduction

Modern naval vessels rely heavily upon acoustic information to determine what is happening in the surrounding ocean. All vessels radiate some noise into the water during their normal operations. This interferes with acoustic sensors both on the ship producing the noise and on nearby vessels. It also increases the probability of detection by passive sonars on opposing vessels. Thus, the understanding and control of the sources of this radiated noise are important naval objectives.

For surface ships, propeller cavitation is often the dominant source of noise, at least at higher operational speeds. Cavitation bubbles form in regions near the propeller where the dynamic pressure is below the vapour pressure of water. These bubbles start as microscopic nuclei which are naturally present in the water, grow to macroscopic size while in the low pressure region, then collapse again after returning to the ambient pressure region. During this life cycle, the bubble volume can change extremely quickly, and so generate a great deal of sound.

The theory describing isolated spherical vapour bubbles is well understood and is sufficient to describe some features of cavitation. Unfortunately, real propeller cavitation is much more complex. Of the different cavitation types, bubble cavitation, which is composed of clusters of small bubbles, is the closest to the ideal isolated bubble model. Other types are quite different. Vortex cavitation is the name for long thin cavities that form in the vortices which extend from the propeller blade tips and hub. Sheet cavitation forms in thin layers starting at the leading edge of propellers. Each of these types of cavitation have different, and as yet poorly understood, mechanisms for producing noise.

This paper describes experiments conducted at Defence Research Establishment Atlantic (DREA) to study the sound source mechanisms of two of these types of cavitation. The tests included extensive measurements of the far-field noise from propellers producing tip vortex and bubble cavitation. These data were then correlated with information about the cavity dynamics, obtained from visual observations.

2 Experiment

The measurements were carried out at the DREA Acoustics Barge. This is a floating laboratory which is located on Bedford Basin, the uppermost part of Halifax Harbour. The water beneath the barge is approximately 50 m deep, and the bottom is covered with several metres of soft mud with good acoustic absorption properties. This provides a non-reverberant, quiet environment for acoustic measurements.

The experimental apparatus was suspended, in open water, below the barge. The propellers were powered by a stationary electric drive system which was fixed to the barge. Visual cavitation observations were made using a video camera, with lighting provided by strobe lights which were synchronized to the propeller rotation. Hydrophones located at several positions around the propellers simultaneously measured the far-field sound at various ranges and angles. The propeller drive system also could be rotated to measure the noise directivity.

item	position (m)		
	x	y	z
propeller ($\theta_d = 0^\circ$)	0.00	1.57	2.59
hydrophone 1	0.99	2.57	2.59
hydrophone 2	0.99	9.14	9.55
hydrophone 3	0.00	17.81	3.15

Table 1: Propeller and hydrophone positions

2.1 Apparatus

Figure 1 shows the experimental set-up under the barge, as well as the system of coordinates. The propeller drive was suspended in the water on a rigid shaft which could rotate through an angle, θ_d , of $\pm 90^\circ$. Throughout most of the experiment, except during the directivity tests, the propeller drive was at the $\theta_d = 0^\circ$ position. Table 1 gives the coordinates of this "standard" propeller location and the three hydrophone locations.

A 40 horsepower, DC electric motor drove the propeller. The rotation rate was variable from 0 to 2500 rpm, and could be held constant within ± 2 rpm using a servo control system. The rotation rate was measured by counting the rate at which the teeth on a 60 toothed wheel, attached to the propeller drive shaft, passed a fixed magnetic proximity sensor.

A video system, similar to that described in Reference [1], recorded instantaneous images of the cavitation. An image processing system later was used to enhance these images and examine certain features in detail.

The acoustic measurements were made with three Brüel & Kjær 8101 hydrophones. The electrical signals from the hydrophones were amplified with Brüel & Kjær 2606 low noise amplifiers, before input to a Hewlett Packard 3562A dual channel signal analyzer which processed all the raw data. The analyzer stored its results on magnetic disks for subsequent post-processing and display by a computer.

Because cavitation noise can be very impulsive, the measurement and analysis instrumentation required both wide frequency response and large dynamic range. The Hewlett Packard 3562A signal analyzer has an analysis frequency range of 0 to 100 kHz and a dynamic range exceeding 80 dB. To fully use these capabilities, only "live" data were processed. This differs from previous cavitation noise experiments at DREA, which used analogue equipment to record the hydrophone signals for later analysis. This was convenient; however, even good quality analogue recorders cannot match the signal analyzer performance. For example, from Reference [2], an IRIG wideband instrumentation recorder at a tape speed of 120 inches per second has a bandwidth of 400 Hz to 2 MHz and a maximum signal to noise ratio of only 30 dB. A typical studio quality audio recorder has better signal to noise ratio, at 55 dB, but the frequency range is only 50 Hz to 15 KHz.

Even with live signals, to use the full dynamic range of the signal analyzer, the input range of each channel must be set so that the maximum hydrophone signal is slightly less than the maximum of the analogue to digital converter. The following two step procedure ensured proper range selection. Immediately before each measurement, the analyzer input range was first set

hydrophone	delay time (mS)		
	direct	surface	barge
1	0.88		
2	6.98	9.78	11.12
3	11.06	11.77	13.33

Table 2: Propagation delay times for the main acoustic paths

so that the hydrophone signal overloaded the instrument. Then the analyzer was placed in "auto-range up" mode, and allowed to automatically increase its range for several seconds until the overloads stopped.

2.2 Calibrations

Free-field calibrations of the hydrophones were conducted at DREA facilities. Brüel & Kjær type 8101 hydrophones, which are cylindrical in shape, are nearly omnidirectional in planes perpendicular to their cylindrical axes; however, they are directional at frequencies above 20 kHz in planes parallel to their axes. All spectra in this paper include a correction for the hydrophone frequency response perpendicular to the axis. No effort was made to compensate for the high frequency directionality, but Section 2.3 considers its effect.

Also, in all results, the hydrophone amplifier gains were assumed to be constant with frequency and equal the values measured at 10 kHz. The gains were obtained from transfer functions for the three amplifiers, measured at each gain setting used in the experiment by injecting a wideband random signal into the amplifier inputs. In all cases, the actual amplifier gains in the frequency range from 100 Hz to 100 kHz were within ± 0.2 dB of the values at 10 kHz.

2.3 Acoustic Environment

Ideally, *free-field* acoustic measurements should include only sound which travels directly from the source to the receiver. Although here the experiment was conducted in open water at the DREA Acoustics Barge, sound still could reflect from the water surface and the underside of the barge.

To examine the multi-path acoustic environment, the propeller was replaced with a spherical piezoelectric acoustic source which was fed a "white noise" electrical signal. Using this, the important acoustic paths were identified with a cross-correlation technique similar to that described in Section 13.2 of Reference [3]. Figure 2 illustrates the method, using results for Hydrophone 3. First, the cross-correlation between the source voltage and the hydrophone output was computed. This is an oscillatory function and its *envelope* gives the desired information. The envelope has peaks at delay times corresponding to the propagation time along each acoustic path. The size of each peak is a measure of the relative amount of sound that travels by the corresponding path. The envelope functions were computed from the cross-correlations by the Hilbert transform method.

Figure 3 shows the cross-correlation envelopes for the three hydrophones and Table 2 summa-

rizes the propagation delays of the important acoustic paths. For Hydrophone 1, the reflections were much smaller than the direct path sound. Thus, Hydrophone 1 measured nearly free-field levels. Hydrophones 2 and 3 received significant reflected sound.

Figures 4 and 5 compare acoustic spectra measured simultaneously at each of the hydrophone locations. These spectral levels, and all others in this paper, are in decibels relative to one micropascal squared in one Hertz bands at one metre. For comparison, the Hydrophone 1 curve is included in both figures.

For Hydrophone 1, the portion of the spectrum above 1 kHz is very close to the free-field transmitting response of the source. Below 1 kHz, the spectrum flattens off, because the sound level of the source dropped below the ambient noise.

The spectra for Hydrophones 2 and 3 are somewhat different. The differences are not caused by the instrumentation, but are solely functions of the positions of the hydrophones. The following items affect these spectra:

1. The signal to noise ratio is lower for hydrophones further from the source. This occurs because the ambient noise is nearly the same at all hydrophones, but the sound from the source decreases with distance. The spectra include the correction

$$- 20 \log(r_d), \quad (1)$$

where r_d is the length of the direct path. This corrects for the range dependence of the sound from the acoustic source, but makes the ambient noise level appear to increase with range. In Figures 4 and 5, this can be seen at low frequency, where the ambient noise dominates the sound from the source.

2. As discussed in Section 2.2, no effort was made to compensate for the directionality of the hydrophones. The direct sound paths to Hydrophones 1 and 3 were nearly 90° to the hydrophone axes, and so the applied hydrophone frequency response correction was sufficient. This was not true for Hydrophone 2, because the direct path to it was at an angle of 47.7° . A free-field hydrophone calibration done at this angle has the same behavior above 20 kHz as shown for Hydrophone 2 in Figure 4. Attempts to apply a correction failed, because the frequency and shape of the dip (at 50 kHz in Figure 4) are very sensitive to the sound path angle and could not be reliably reproduced during the calibration.
3. The spectra for Hydrophones 2 and 3 show effects caused by multi-path sound transmission. As shown in Figure 3, these hydrophones had two significant reflected paths. Thus, the measured acoustic pressure, P , is related to the free field acoustic pressure, P_f , by

$$P(t) = P_f(t - \tau_d) + A_s P_f(t - \tau_s) + A_b P_f(t - \tau_b). \quad (2)$$

Here, τ_d , τ_s , and τ_b are the propagation delays of the direct path, surface reflection, and barge reflection. The quantities A_s and A_b are the corresponding strengths of the reflections, relative to the direct path sound level. The large impedance mismatch at the water-air interface causes nearly perfect reflection with a phase inversion, and so $A_s = -r_d/r_s$. Reflection strength A_b also is proportional to the ratio of path lengths, r_d/r_b , but the acoustic properties of the water-barge interface are much more complex. Thus, A_b probably is a function of frequency.

From Equation 2, the measured spectral density, S , is related to the free-field spectral density, S_f , by

$$S(\omega) = \left\{ 1 + A_s^2 + A_b^2 + 2A_s \cos[\omega(\tau_s - \tau_d)] + 2A_b \cos[\omega(\tau_b - \tau_d)] + 2A_s A_b \cos[\omega(\tau_b - \tau_s)] \right\} S_f(\omega). \quad (3)$$

The cosine terms in this equation explain the ripples in the Hydrophone 2 and 3 spectra. Spectra with bandwidths that are proportional to frequency, as in Figures 4 and 5, show these ripples only at low frequencies where the bandwidth is small. At high frequencies, where the bandwidth is large, the Hydrophone 2 and 3 spectra are simply offset from the free-field levels, by the amount given by the A_s^2 and A_b^2 terms.

The presence of the propeller drive did not significantly affect the acoustic measurements. This was confirmed by attaching the source, first to the propeller drive shaft, and later suspending it at the same location with the drive removed.

Based on the results of this study of the multi-path acoustic environment, the three hydrophones were used as follows:

1. Hydrophone 1 was used for all measurements, except for directivity. It gave nearly free-field levels and had the best acoustic signal to noise ratio. It was located a bit too close to the propeller to be considered in the far-field at low frequencies, but still the results compared very well with those from the other hydrophones.
2. Hydrophone 2 was used for quality control.
3. Hydrophone 3 was used for the directivity measurements.

3 Propellers

A number of propellers have been tested at the above facility, but results are given here only for three which illustrate behavior typical of tip vortex and bubble types of cavitation. These propellers also were used for the work reported in References [4, 5].

Figure 6 shows the propeller blade outlines, as well as the cavitation patterns. The propellers were two bladed, of 250 mm diameter, and were designed to produce specific types of cavitation under the experimental conditions. They had a NACA 16 thickness distribution and a NACA 65 mean camber line; however, the radial distributions of pitch, chord length, maximum thickness, and maximum camber were different.

The first propeller, called Tip Vortex 1 (TV1), had a circulation distribution that peaked relatively near the tip, and so produced a strong tip vortex. Tip vortex cavitation began at approximately 600 rpm. Near the inception speed, the cavitation appeared as thin strands extending behind, but not actually touching, the blade tips. With increasing speed, the tip vortex cavities developed an oval shaped disturbance, giving them the appearance of thick spiral ribbons. This remained the only type of cavitation to approximately 2000 rpm, when a small amount of bubble cavitation began to form at mid-chord near the tips. This fed free bubbles into the vortex giving it a fluffy appearance, although the vortex remained clearly discernible up to the maximum speed of 2500 rpm.

The second propeller, referred to as Back Bubble (BB), had a circulation which peaked nearer center span, and so produced a weaker tip vortex. Also, Propeller BB had thicker blades with greater camber to encourage the development of bubble cavitation. This propeller began to produce tip vortex cavitation at approximately 500 rpm. This cavitation looked similar to that produced by Propeller TV1, but was less intense. Mid-chord bubble cavitation began at 1430 rpm. Initially this made the tip vortex cavitation appear fluffy, but by 2000 rpm the vortex had disappeared completely, leaving only bubble cavitation. A small amount of hub vortex cavitation also was present at speeds above 1300 rpm.

The final propeller, called Tip Vortex 2 (TV2), had a similar circulation distribution to Propeller BB, but had thinner blades and less camber. It produced tip vortex cavitation first at 800 rpm. Above 1300 rpm a small amount of intermittent hub vortex cavitation also was present. Unfortunately, due to equipment failure during the series of experiments reported here, comparatively few measurements were made with Propeller TV2.

4 Cavitation Noise Spectra

The spectral density of the far-field sound from these propellers was measured, from 0 to 100 kHz, at various propeller speeds. All spectral levels are in decibels relative to one micro-pascal squared in one Hertz bands at one metre.

4.1 Propeller TV1

Figures 7 and 8 show how the spectral density of the far-field noise from propeller TV1 varied with frequency and propeller speed. The low frequency portions of the spectra are quite complex, as Figure 7 shows, and are discussed in detail later; however, at high frequencies the spectra are relatively simple and generally fall off with frequency at some nearly constant rate which depends upon propeller speed.

Propeller TV1 produced three distinct types of cavitation noise in different speed ranges. Figure 8 illustrates this by showing the speed variation of the 10 kHz noise. Speed range I goes from the cavitation inception speed of 600 rpm to 1300 rpm, range II from 1300 rpm to 2000 rpm, and range III from 2000 rpm to the top speed of 2500 rpm.

At the cavitation inception speed, broadband noise first appeared above the background in the frequency band from 10 kHz to 100 kHz. (The background noise, shown as the 500 rpm curve in Figure 7, was mainly from the propeller drive machinery.) As the propeller speed increased into region I, the spectral peak moved to lower frequencies and the slope of the high frequency spectrum increased from approximately -7 dB per octave at inception, to almost zero between 1000 rpm and 1200 rpm.

When the speed entered region II, the character of the noise suddenly changed. In going from 1200 rpm to 1400 rpm, the slope of the high frequency spectrum decreased to -5 dB per octave, resulting in a reduction in noise above 6 kHz. In addition, strong narrowband noise developed at low frequencies. This behavior continued throughout region II. The maximum noise output from this propeller was at 1800 rpm, reaching 180 dB in the 100 Hz to 100 kHz band.

At the beginning of speed region III, the intense low frequency narrowband noise stopped. In addition, the noise levels at all frequencies decreased from the maximum at 1800 rpm.

As mentioned above, the cavitation noise spectra for propeller TV1 are quite complex at low frequencies. Figure 9 shows several 0 to 1 kHz spectra in detail. The curves at 1000 rpm and 1200 rpm are results from propeller speed range I. These spectra have two peaks caused by the cavitation noise, labeled *a* and *b* in the figure. The peaks move to lower frequency with increasing speed, and the ratio of the peak frequencies, f_b/f_a , is approximately 1.4. The 1400, 1600, and 1800 rpm spectra are from speed region II. These spectra also have a small low frequency peak with the same character as peak *a* at lower speeds, but the dominant feature is the group of high intensity peaks which replace peak *b*. The largest peak usually occurs between $1.4f_a$ and $1.6f_a$, with neighbouring peaks separated by multiples of the propeller rotational speed. In addition, another pair of smaller peaks appear between $3.0f_a$ and $3.5f_a$. At the highest propeller speeds, the low frequency spectra revert to the dual peaked structure, except that the peaks move to higher frequency with increasing propeller speed.

Peak *a* occurred in all of the low frequency cavitation noise spectra. Figure 10 shows the variation of f_a with propeller speed. The frequency of peak *a* dropped smoothly with increasing speed through speed ranges I and II, and then increased somewhat in range III.

4.2 Propeller BB

Propeller BB developed cavitation noise which was similar to that just described, but with a number of subtle differences. Figure 11 shows far-field noise spectra from 100 Hz to 100 kHz at various propeller speeds, while Figure 12 shows the low frequency spectra at high resolution. As for the previous propeller, cavitation noise first appeared above the background noise at high frequencies, but the slope of the high frequency spectra changed comparatively little with increased speed. The slope at 10 kHz remained between -6 and -7 dB per octave from 600 rpm to 1400 rpm; however, the low frequency spectra in this speed range were similar to those of Propeller TV1. Again the spectra have two peaks (labeled *a* and *b* in Figure 12), with $f_b/f_a \approx 1.4$. At 1500 rpm, Propeller BB developed intense narrowband noise which was very similar to that produced by Propeller TV1, but this disappeared again by 1600 rpm. Above 1600 rpm, the spectra became quite smooth.

Figure 13 shows how the intense peaks develop between 1400 and 1500 rpm. Three distinct peaks form between 250 and 300 Hz. At 1475 and 1500 rpm, these peaks are separated by exactly the propeller rotation frequency.

4.3 Propeller TV2

Comparatively few data were obtained for Propeller TV2 because equipment failure greatly limited the maximum stable propeller speed. Spectra were obtained at low speeds, and again the tip vortex cavitation produced noise with the dual peaked spectral structure. Figures 14 and 15 show these results.

5 Cavitation Noise Directivity

5.1 Propeller TV1

All the results in Section 4 were measured using Hydrophone 1 at an angle, θ , of 45° from the downstream propeller axis. The noise measured by Hydrophone 3, at an angle of approx-

imately 0°, was somewhat different. Figure 16 compares spectra measured simultaneously by Hydrophones 1 and 3, at several propeller speeds. Near the cavitation inception speed, the two hydrophones gave results that agree (within the tolerances described in Section 2.3). As the speed increased and the cavitation became more intense, the spectra from the two hydrophones began to differ in a way that depended upon frequency. The Hydrophone 3 sound levels increased between 300 Hz and 6 kHz, relative to Hydrophone 1, while the opposite was true at frequencies above 10 kHz.

This behavior was due to directivity of the cavitation noise. To prove it, a set of directivity measurements were made with Propeller TV1 at 2500 rpm, by rotating the propeller drive motor and measuring the noise with Hydrophone 3. Figure 17 compares a spectrum measured broadside to the propeller ($\theta = 90^\circ$) with one directly downstream ($\theta = 0^\circ$). As before, moving into the downstream sector caused a reduction in high frequency noise, as well as an increase in noise between 300 Hz and 6 kHz. Also, the downstream spectrum lost the characteristic ripples caused by multi-path acoustic propagation.

Figure 18 shows how the sound varied with angle. To remove effects due to multi-path acoustic propagation, the spectra were averaged over frequency using

$$\bar{S} = \frac{1}{f_u - f_l} \int_{f_l}^{f_u} S(f) df, \quad (4)$$

where f_l and f_u are the lower and upper edges of the averaging band. Figure 18 includes two sets of results, one averaged from 1 to 5 kHz and the other from 40 to 45 kHz. These show that the cavitation noise from Propeller TV1 changed very little over angles from 20° to 90°, but was directional in the sector within 20° of the downstream propeller axis.

5.2 Propeller BB

The directional properties of cavitation noise from Propeller BB were similar to those just described. Figure 19 compares spectra measured with Hydrophones 1 and 3 at various propeller speeds. Figures 20 and 21 show the directivity at 1400 rpm, and Figures 22 and 23 show it at 2000 rpm. As found for Propeller TV1, the cavitation noise from Propeller BB had the following directional characteristics.

1. The directionality increased as the propeller speed and the amount of cavitation increased.
2. The directionality was confined to a sector within 20° of the downstream propeller axis.
3. In the downstream sector, the spectral levels from 300 Hz to 10 kHz increased, but above 10 kHz the levels decreased.
4. In the downstream sector, the multi-path effects decreased.

6 Cavitation Noise Waveform Analysis

Finally, some analysis was done on the cavitation noise waveforms. The original intent of this was to analyze the acoustic pulses produced by individual cavitation bubble implosions. Unfortunately, this type of waveform was rare. Most of the cavitation produced noise without isolatable pulses, at least not with the 100 kHz analysis system used here.

It proved more useful to study the probability density function of the acoustic pressure, $F_P(P)$. Using the analysis that will now be described, this can provide information about the overall structure of the acoustic waveform, as well as about the acoustic pulses.

The shape of the probability density function contains the desired information. Thus, to make comparisons at different propeller speeds, it is convenient to transform the argument of the experimental probability density function to

$$P' = \frac{P - \bar{P}}{s}, \quad (5)$$

where \bar{P} and s are estimates of the mean and standard deviation of the acoustic pressure. The experimental values of $F_P(P)$ were measured with a Hewlett Packard 3562A signal analyzer using AC input coupling. Thus, the mean was automatically removed. The standard deviation was computed from the measured probability density using

$$s^2 = \int_{-\infty}^{+\infty} P^2 F_P(P) dP. \quad (6)$$

Transformation to P' also requires that the probability density function be renormalized to

$$F_{P'}(P') = s F_P(P). \quad (7)$$

The *normal* probability density function describes many random processes. If this also is true here, then $F_{P'}$ will equal the standard normal function,

$$N_{P'}(P') \equiv \frac{1}{\sqrt{2\pi}} \exp\left(-\frac{P'^2}{2}\right). \quad (8)$$

In many cases $F_{P'}$ did closely approximate $N_{P'}$. Those differences that did occur were at large values of $\pm P'$, where $F_{P'}$ sometimes greatly exceeded $N_{P'}$. This increase in the probability of obtaining high acoustic pressures indicates that impulsive noise was being produced. To detect this effect better, it is convenient to work with the logarithm of the probability density functions. This also gives the standard normal function the very simple form

$$\log_{10} [N_{P'}(P')] = -0.399 - 0.217 P'^2. \quad (9)$$

Figure 24 compares $\log(F_{P'})$ with $\log(N_{P'})$, for Propeller TV1 at several speeds. At 1000 rpm, this propeller did produce distinct acoustic pulses and this shows up as a relatively broad and symmetric normalized probability density. These distinct pulses stopped at higher propeller speeds, although at 2000 rpm the $\log(F_{P'})$ curve indicates that there were some impulses which were predominately in the direction of positive pressure. At the highest speed, 2500 rpm, the probability density closely approximates the normal distribution.

Probability densities were also measured for Propellers TV2 and BB at a few speeds, and generally were very close to the normal distribution.

7 Discussion

7.1 Tip Vortex Cavitation

Both Propellers TV1 and BB produced tip vortex cavitation alone over a substantial speed range: in both cases the low frequency cavitation noise developed the same way. At low speeds, there were two small spectral peaks which occurred at frequencies in a ratio of 1.4. (Propeller TV2 also had this behavior over the limited speed range for which tests were done.) At higher speeds, a group of strong narrowband peaks replaced the higher frequency small peak. Both of these behaviors seem to be related to disturbances which develop on the surface of tip vortex cavities.

7.1.1 Low Intensity Modes

Many years ago, Lord Kelvin [6] predicted that discrete vibrational modes should occur on the surface of an infinitely long vortex cavity in an incompressible liquid. In recent years, others (for example see References [7, 8, 9, 10]) extended the theory to include the effects of compressibility, viscosity, and the helical shape of propeller tip vortices. Unfortunately, to the author's knowledge, there has been little experimental confirmation of these results.

Morozov [8] showed that a straight vortex cavity in an incompressible liquid can have an axisymmetric mode with a wave number k given by

$$\ln(ka) = - \left(\frac{M}{ka} \right)^2, \quad (10)$$

where M is the Mach number of the liquid at the surface of the cavity and a is the radius of the cavity. The pressure in the vortex cavity is approximately the vapour pressure of water, p_v , and so from the Bernoulli equation, the liquid velocity at the surface of the vortex is

$$u_\theta = \sqrt{\frac{2(p_0 - p_v)}{\rho}}. \quad (11)$$

Here, ρ is the density of the water and p_0 is the static pressure that would exist at the location of the vortex, if it did not exist. In this experiment, p_0 is the atmospheric pressure plus the head due to the depth of the propeller below the water surface, so that $M = 0.0106$. Using this, numerical solution of Equation 10 gives $ka = 0.0046$ for the axisymmetric mode.

Other non-axisymmetric modes should occur at

$$ka = (m \pm \sqrt{m}) M, \quad m = 1, 2, \dots \quad (12)$$

The $m = 1$ mode describes a serpentine motion, whereas for $m = 2$ the vortex cavity cross-section is elliptical. The two frequencies for each value of m correspond to two modes of the same shape which travel around the vortex at different speeds, but both in the direction of rotation of the liquid [7].

Equations 10 and 12 show that the modal frequencies occur in certain ratios which are independent of the cavity radius. Table 3 gives the ratios of the first three non-axisymmetric modal frequencies, f_m , over the symmetric modal frequency, f_0 .

The ratio of the two lowest frequency modes is 1.4, which also is the frequency ratio of the two spectral peaks in the experimental data at low propeller speeds. This suggests that

m	f_m / f_0	
	lower	upper
1		4.6
2	1.4	7.9
3	2.9	10.9

Table 3: Ratios of vortex cavity modal frequencies

these peaks are caused by the axisymmetric mode and the lower frequency $m = 2$ mode. This hypothesis is supported by photographs, which clearly show that the vortex cavity has the twisted elliptical shape of the $m = 2$ mode. The number of twists of the vortex shape per propeller turn corresponds to the second spectral peak frequency. In addition, the observed cavity radii are of the magnitude predicted by the above theory using the experimental peak frequencies as the modal frequencies.

7.1.2 High Intensity Modes

The behavior described above was present at propeller speeds from tip vortex cavitation inception up to some critical value. Above this speed, the spectral peak associated with the axisymmetric cavity mode remained, but the $m = 2$ peak was replaced by a group of intense narrowband peaks. To the author's knowledge, no existing theory predicts this effect.

An interesting feature of these spectra is that most of the peaks in the group are separated by multiples of the propeller rotation frequency. Whatever events cause this must happen once per propeller turn; however, the propellers had two virtually identical blades, and so symmetry would seem to require the peak spacing to be twice the rotation frequency. Photographs of cavitation near the blade tips gave no indication of the reasons for this behavior, but others showing the downstream portions of the vortex suggest the following explanation.

Near the propeller blades, the tip vortices must follow the helical paths imposed by the cylindrical symmetry and the flow through the propeller. The liquid in both vortices rotates in the same direction; and so, far downstream, their interaction will make them twist about each other in way that depends only upon their strengths. The photographs clearly show this behavior. At low propeller speeds, the vortices are weak and the vortex cavities retain their helical shape. Higher speed increases the vortex strength, causing greater interaction and longer cavities. This makes the downstream ends of the vortex cavities twist tightly together. The combined vortex pair then rotates at the propeller rotation frequency.

7.2 Bubble Cavitation

Propellers TV1 and BB produced bubble cavitation which began near the blade tips at mid-chord and fed free bubbles into the tip vortices. Small amounts of bubble cavitation appear to greatly affect tip vortex cavitation noise. The intense narrowband noise stopped at speeds just above bubble cavitation inception and was replaced by noise with double spectral peaks, similar to that characteristic of low speed tip vortex cavitation noise. As the speed increased further, the bubble cavitation affected the two propellers differently.

The tip vortex cavities of Propeller TV1 remained intact up to the maximum speed. The amount of bubble cavitation apparently was not sufficient to produce detectable noise on its own. Bubble cavitation did affect the noise source mechanisms of the tip vortex cavitation such that the noise at all frequencies was reduced.

Propeller BB produced much more bubble cavitation at high speeds. When the bubble cavitation became intense, the tip vortex cavities disappeared. The noise from this "pure" bubble cavitation had a smooth spectrum, without the characteristic features of tip vortex cavitation noise.

7.3 Cavitation Noise Directivity

The cavitation noise from Propellers TV1 and BB had the directional characteristics summarized in Section 5.2. The effect was greatest in the sector within 20° of the downstream propeller axis. Noise from this sector must have propagated through the propeller wake. Assuming behavior similar to a submerged turbulent jet, the wake should have been confined inside a 15° divergent cone [11]. This volume of liquid would contain many small gas bubbles, produced by diffusion of dissolved gas into the large cavitation bubbles. Even a small quantity of bubbles can greatly increase the acoustic attenuation and decrease the phase speed.

Although detailed calculations cannot be made because the bubble size distribution in the wake is unknown, the above changes in the acoustic propagation properties of the wake could explain the observed directivity. Visual observations of the wake showed that it contained many small bubbles which would attenuate high frequency sound very effectively. In addition, the reduced sound speed in the wake would cause an acoustic impedance mismatch at the wake surface. This would cause the wake to act like a waveguide for sound produced in the wake, and could explain the increase in low frequency sound on the propeller axis.

8 Concluding Remarks

This paper described an experiment designed to examine how different types of propeller cavitation produce noise. The results, measured under nearly free-field conditions, show the spectral characteristics and waveform of the far-field noise at different stages of cavitation development.

Two characteristic types of spectra occurred when only tip vortex cavitation was present. At low propeller speeds, two spectral peaks occurred which correlate well with the two lowest frequency modes of vibration of the cavity surface. At higher speeds, intense narrowband noise occurred which can be related to interaction between the tip vortex cavities at their downstream ends.

Even small amounts of bubble cavitation greatly affect tip vortex cavitation noise, if the free bubbles feed into the vortices. Bubble cavitation by itself, without other types of cavitation, produced noise with a smooth spectrum.

The cavitation noise was directional at angles where the sound must propagate through the propeller wake. The observed effects are consistent with those expected for a wake containing many small bubbles, probably caused by diffusion of dissolved gas into the cavitation bubbles.

Finally, a method for waveform analysis was described, using measurements of the probability density of the acoustic pressure. This technique showed that the waveform of the cavitation noise

often did not contain distinct pulses. Instead, the waveform usually was a random function that was very closely described by the normal probability density.

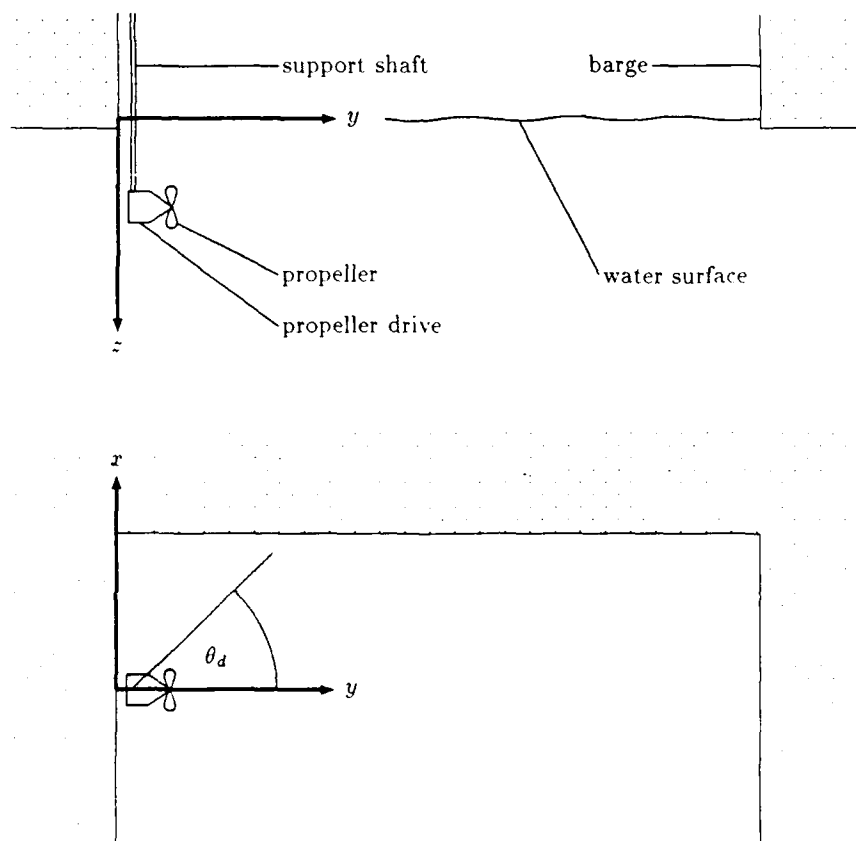


Figure 1: Experimental set-up

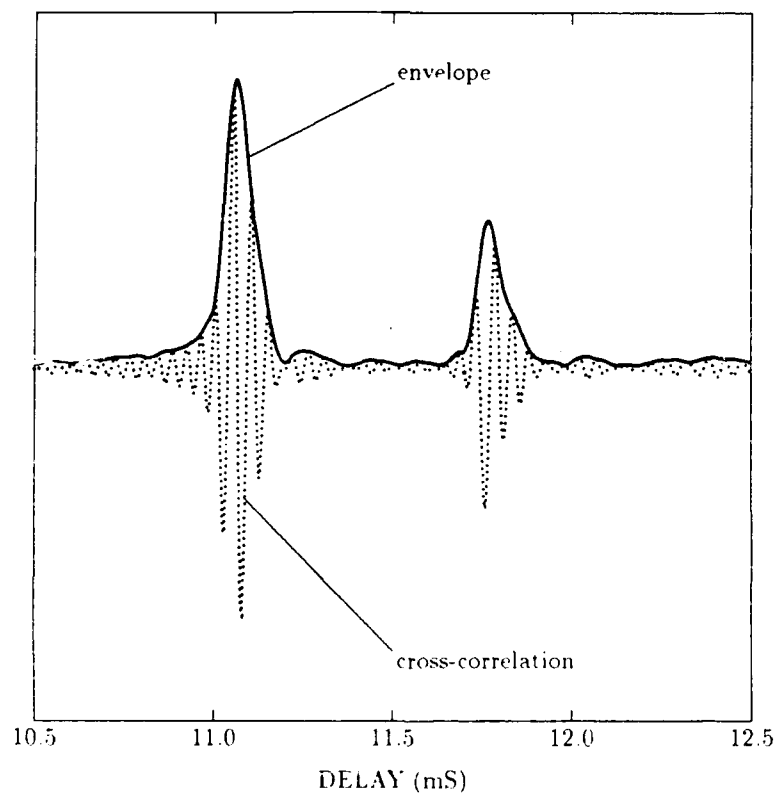


Figure 2: Cross-correlation function and its envelope

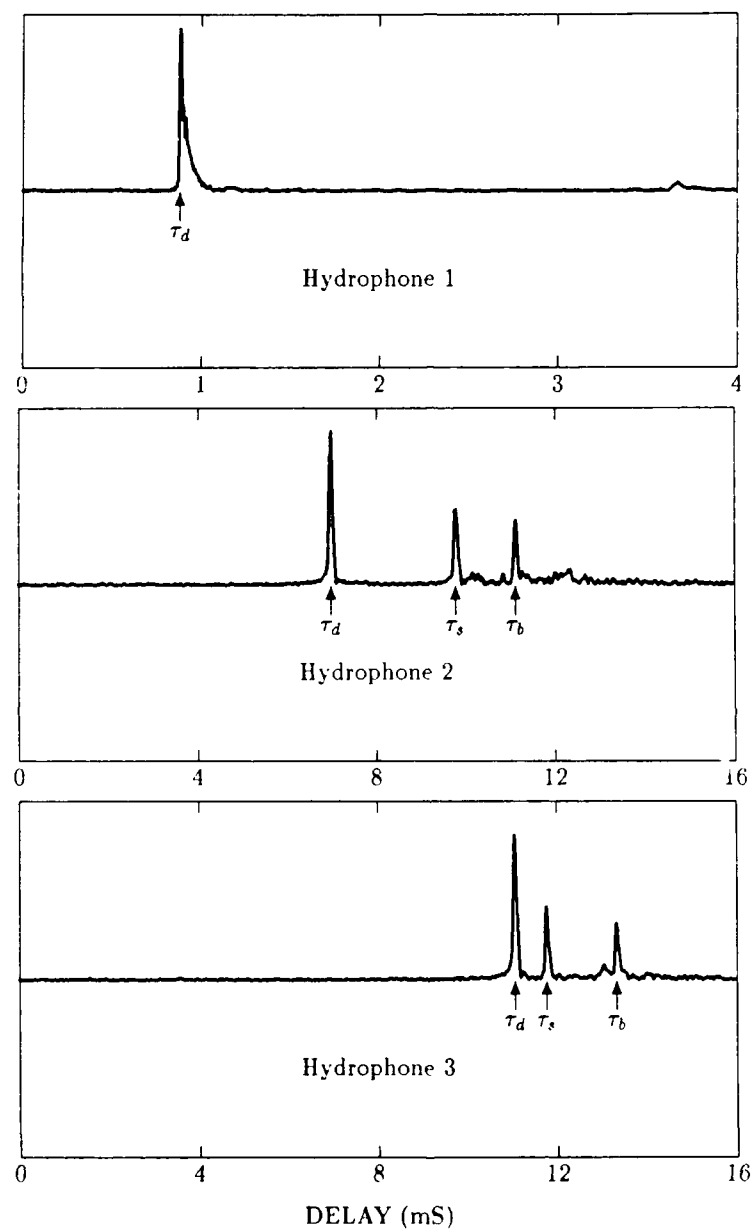


Figure 3: Cross-correlation envelopes

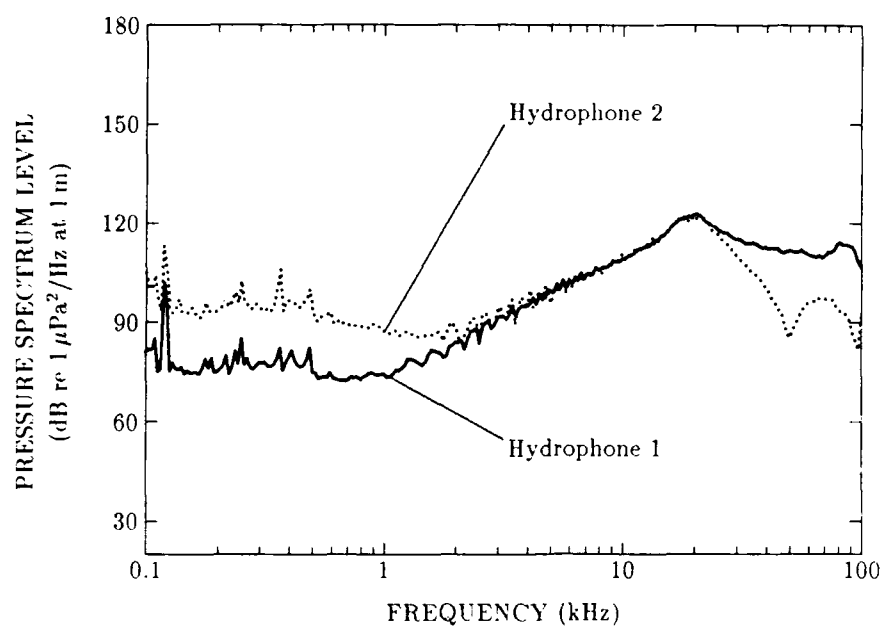


Figure 4: Comparison of spectra measured by Hydrophones 1 and 2

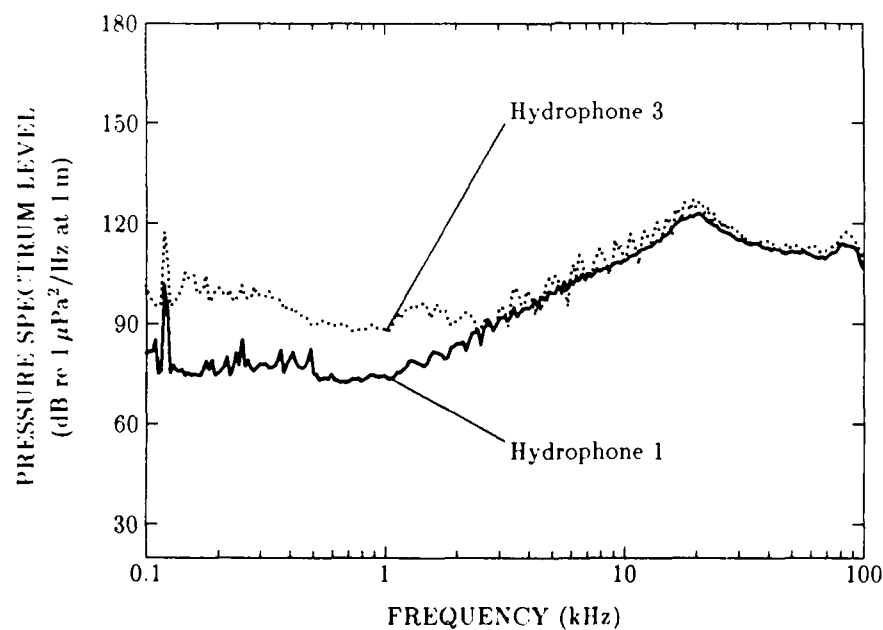


Figure 5: Comparison of spectra measured by Hydrophones 1 and 3

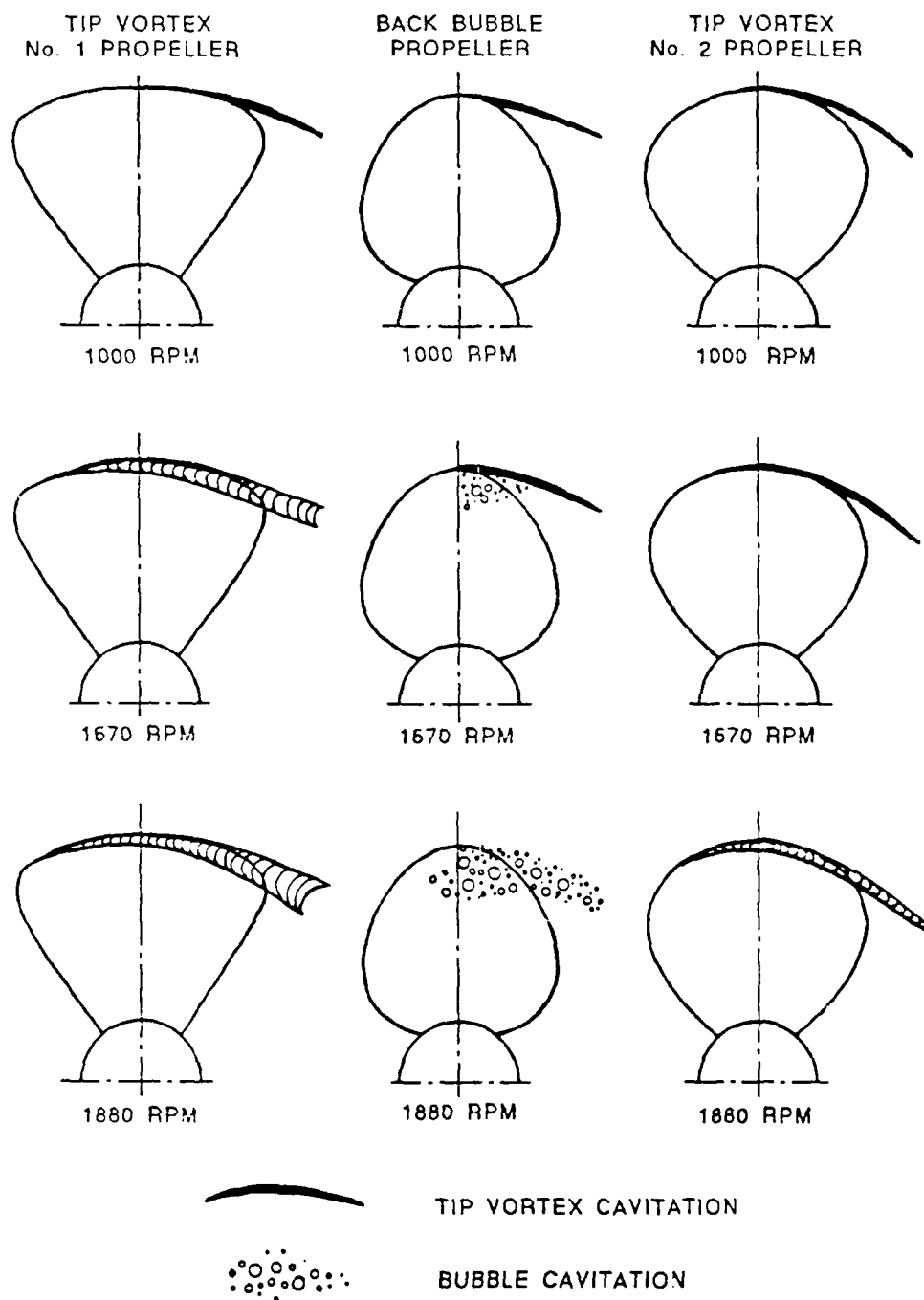


Figure 6: Propeller outlines and cavitation patterns

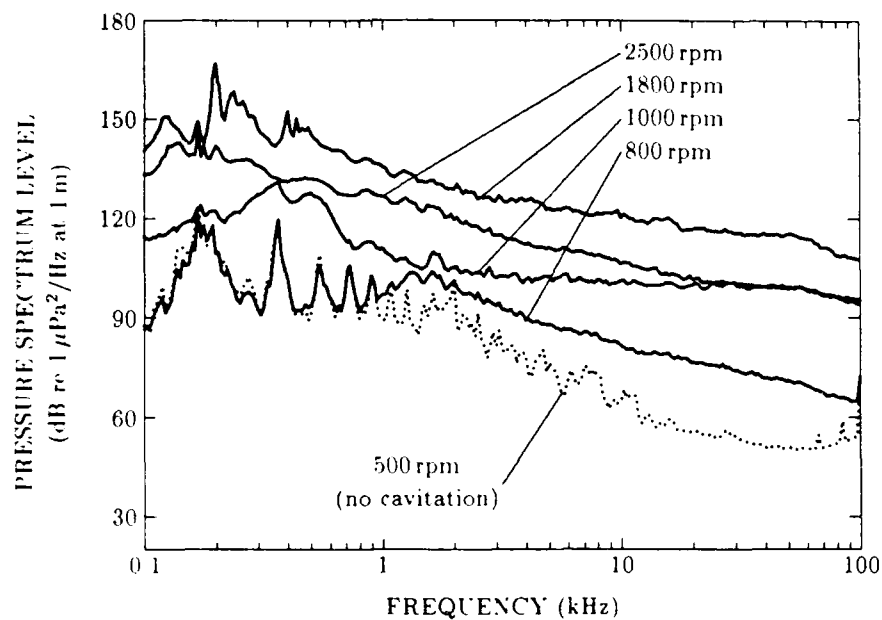


Figure 7: Spectral density of noise from Propeller TV1

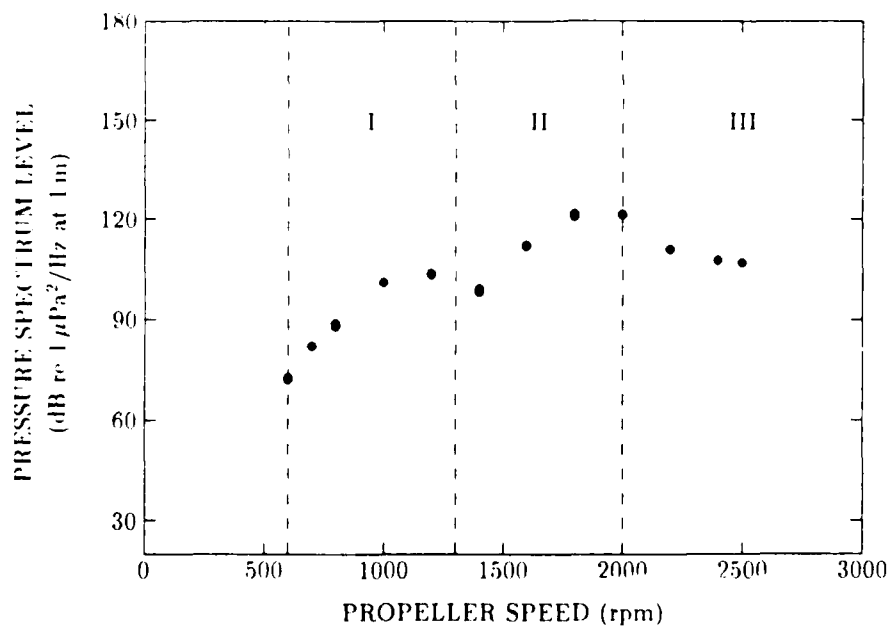


Figure 8: Speed variation of 10 kHz noise from Propeller TV1

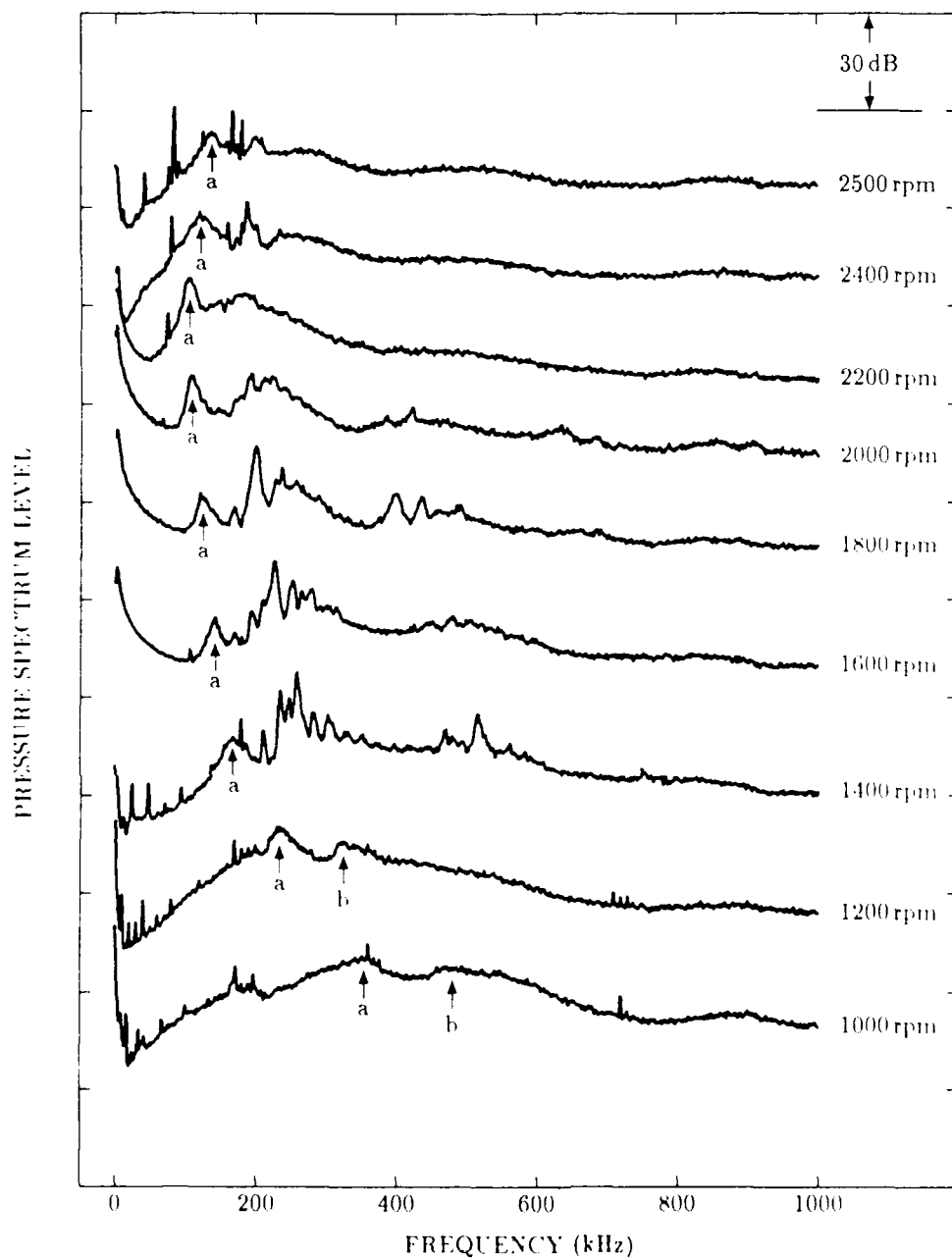


Figure 9: Low frequency spectra for Propeller TV1. Each curve is offset by 30 dB for clarity.

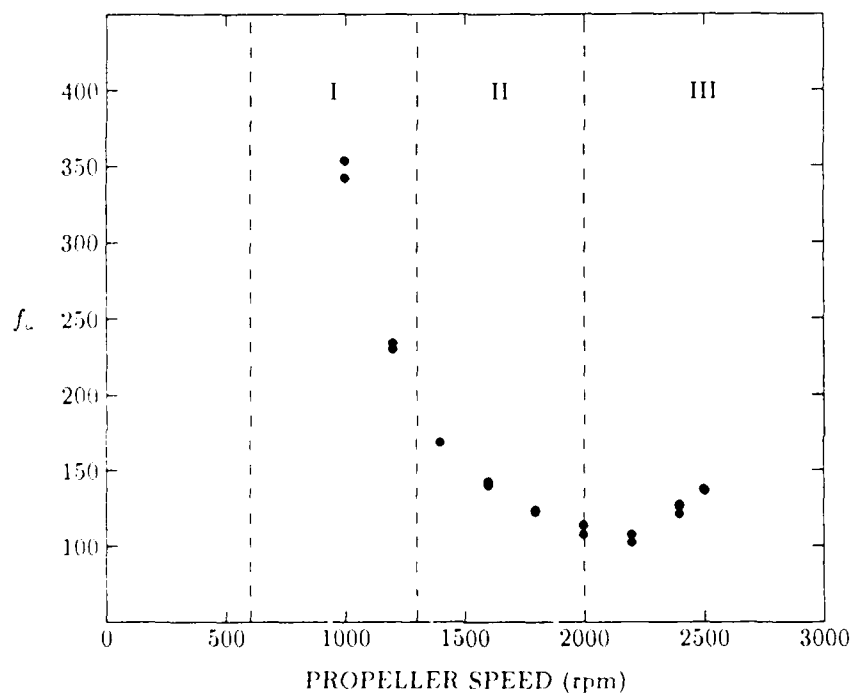


Figure 10: Variation of f_n with rotation rate, for Propeller TV1

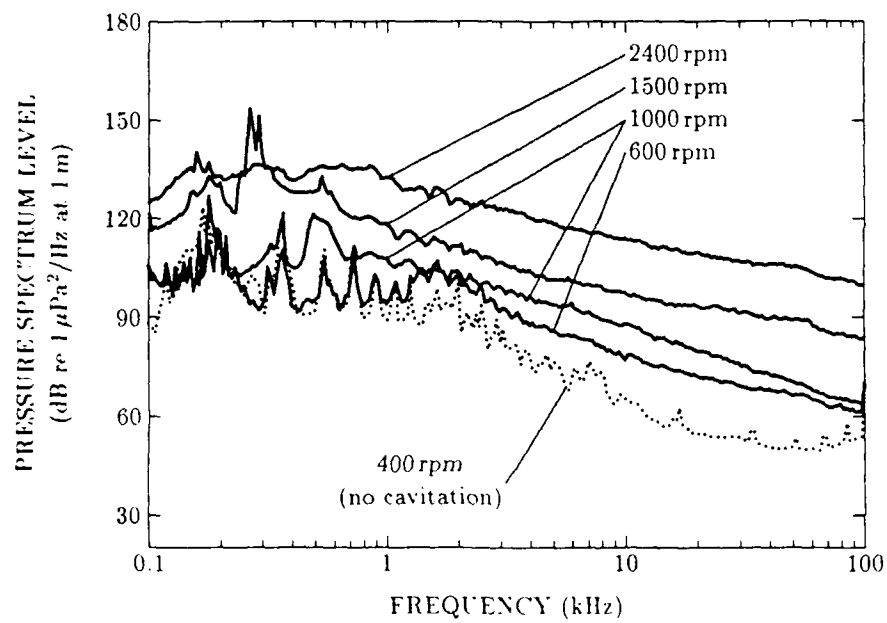


Figure 11: Spectral density of noise from Propeller BB at several speeds

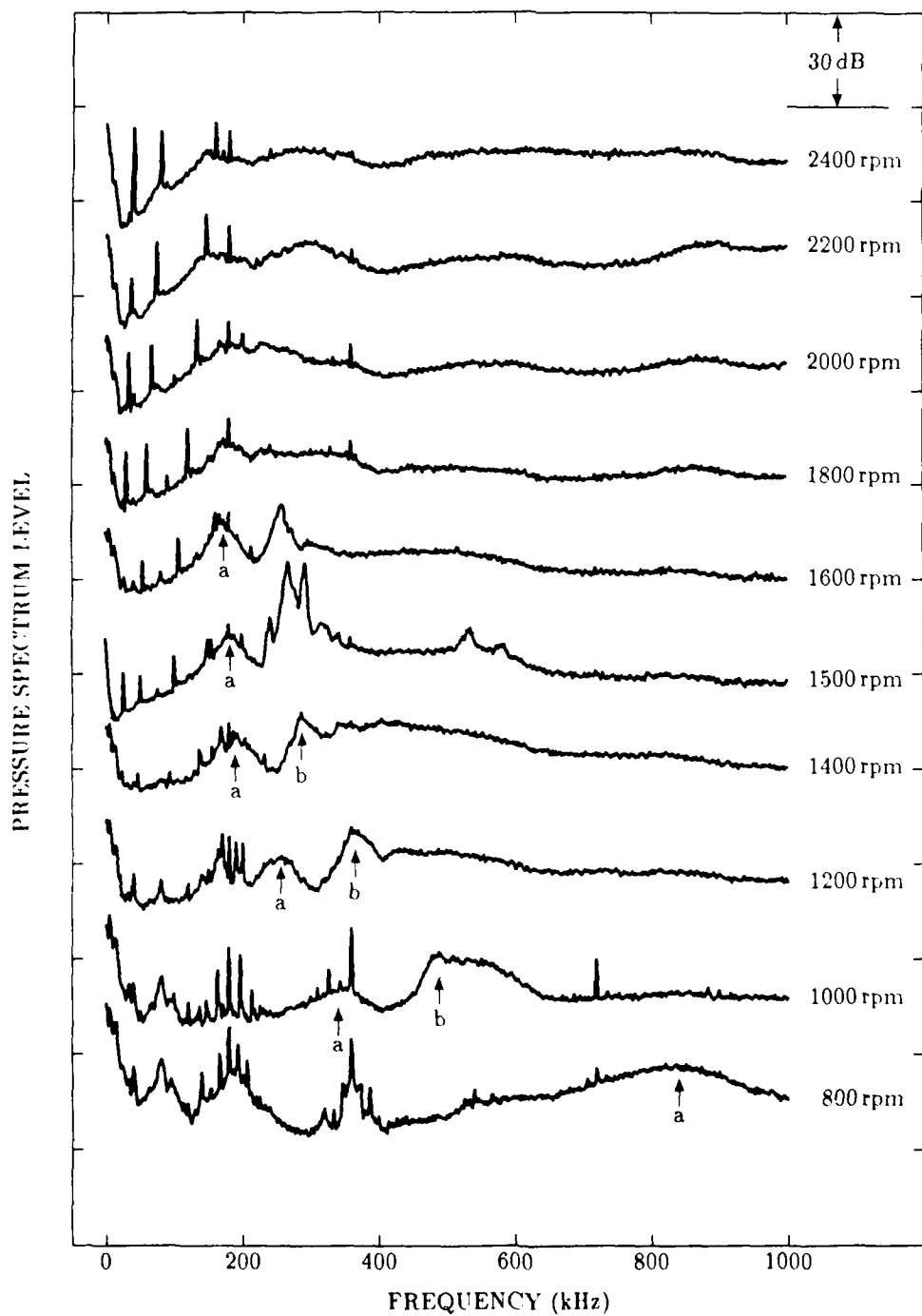


Figure 12: Low frequency spectra for Propeller BB. Each curve is offset by 30 dB for clarity.

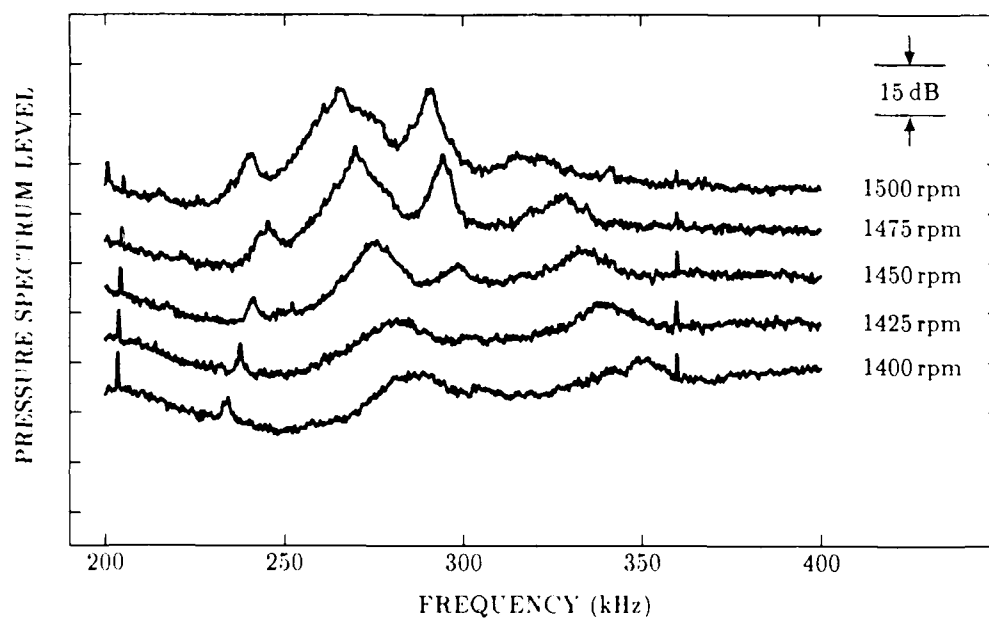


Figure 13: Peak development for Propeller BB. Each curve is offset by 15 dB for clarity.

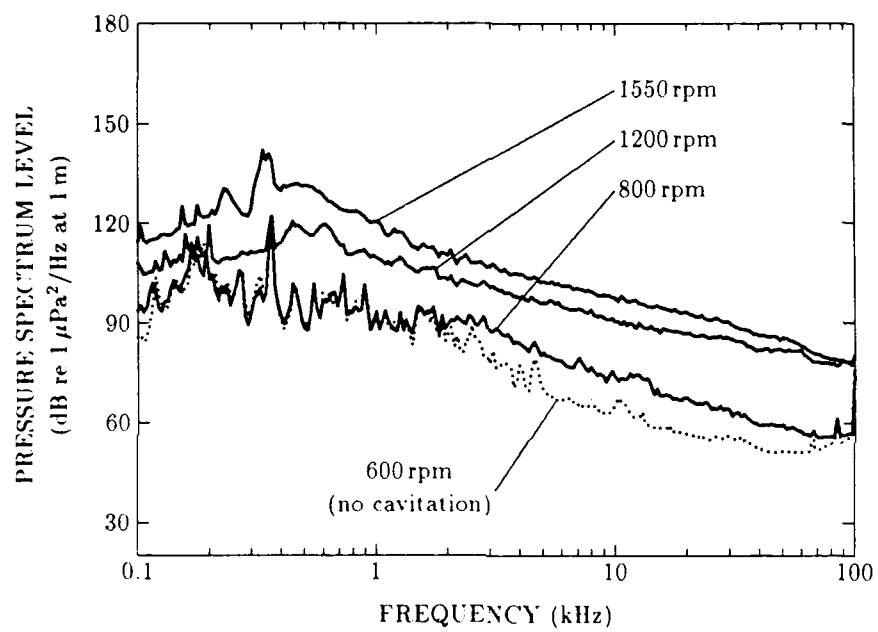


Figure 14: Spectral density of noise from Propeller TV2 at several speeds

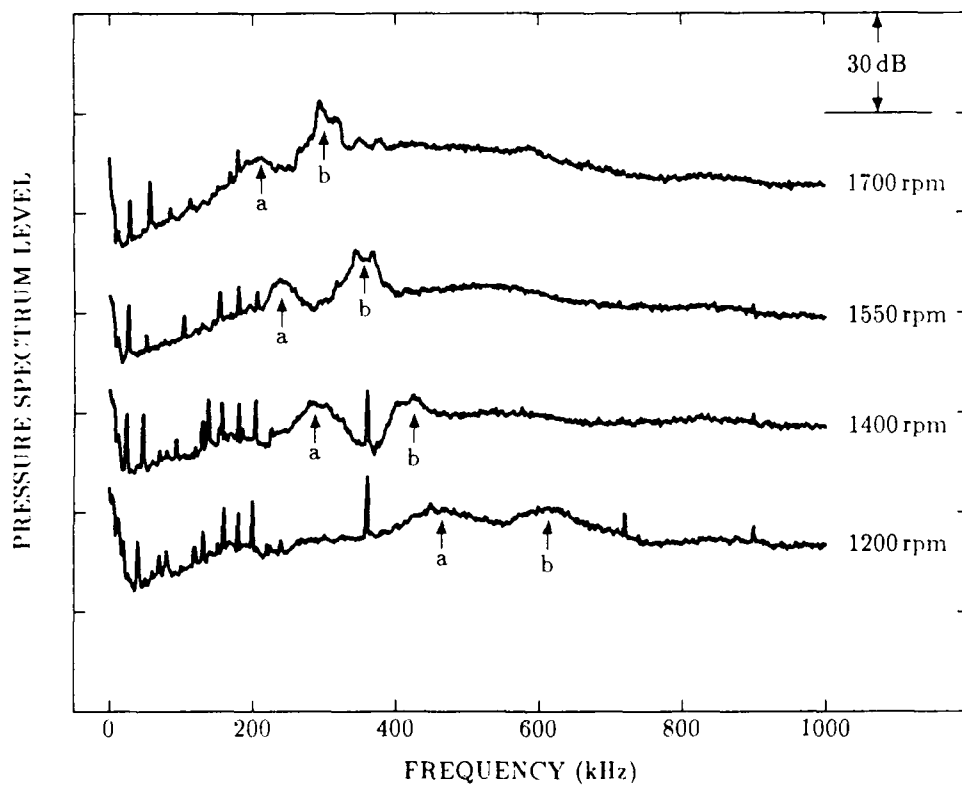


Figure 15: Low frequency spectra for Propeller TV2. Each curve is offset by 30 dB for clarity.

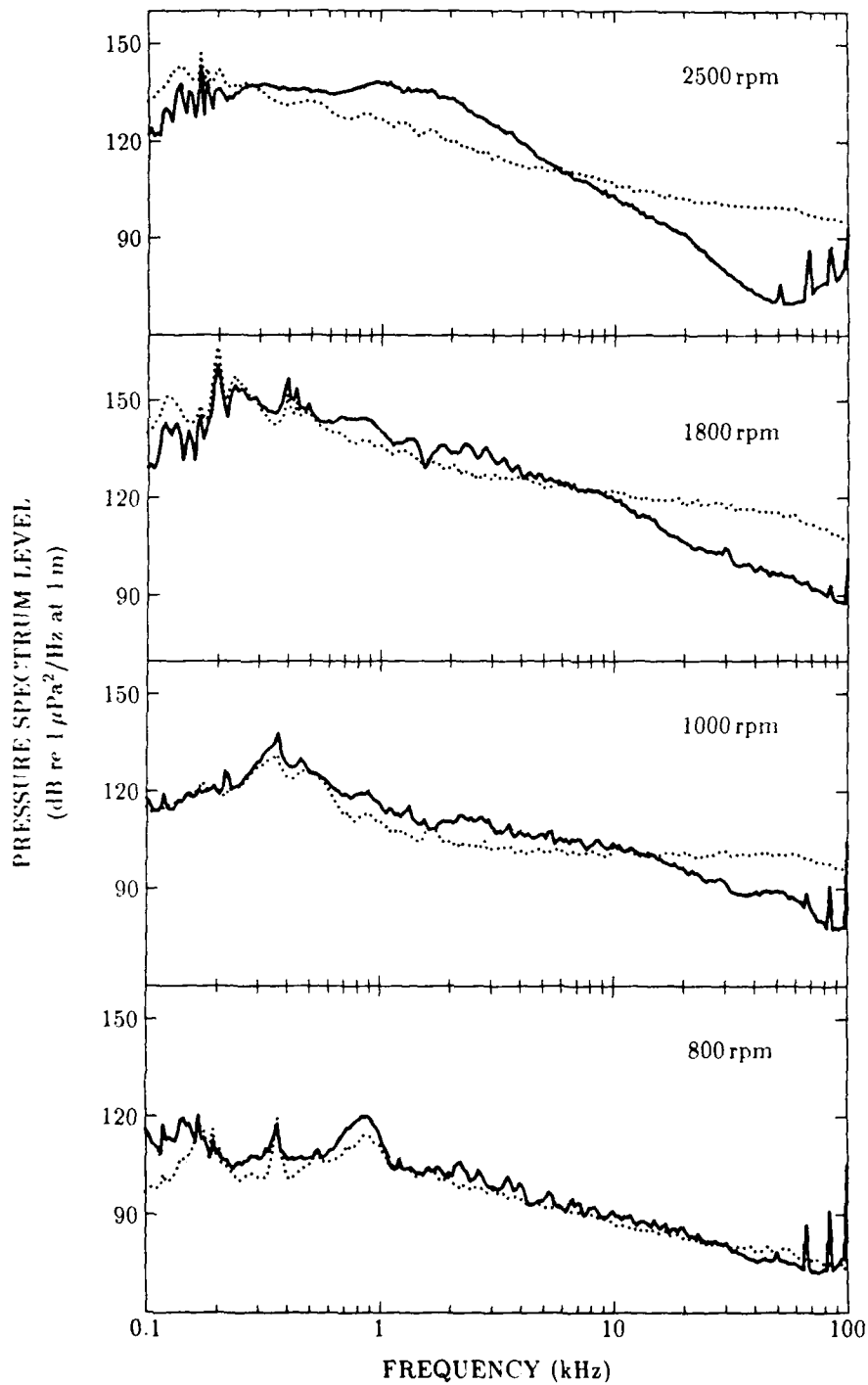


Figure 16: Comparison of spectra measured with Hydrophones 1 (dotted lines) and 3 (solid lines), for Propeller TV1, at various rotation rates

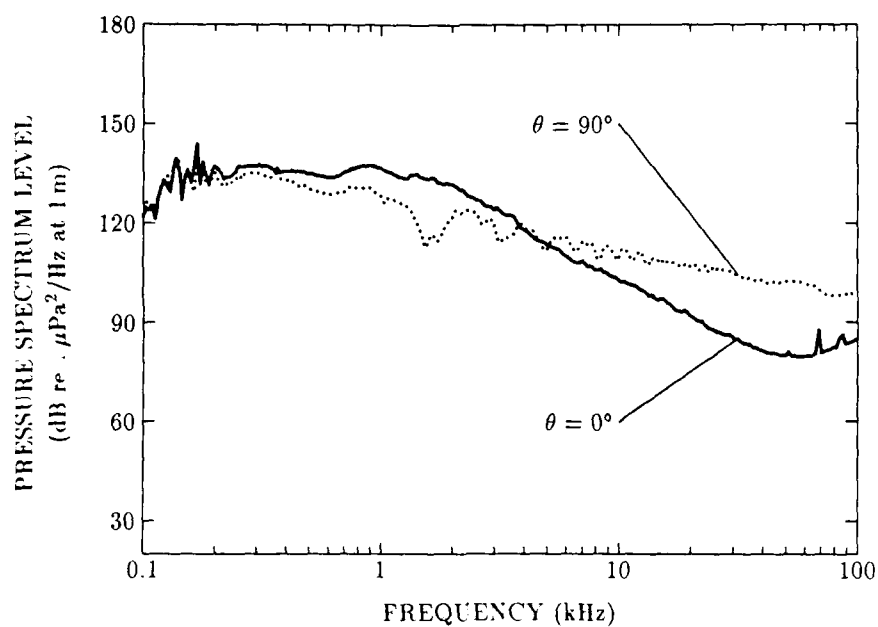


Figure 17: Comparison of spectra at $\theta = 0^\circ$ and 90° for Propeller TV1 at 2500 rpm

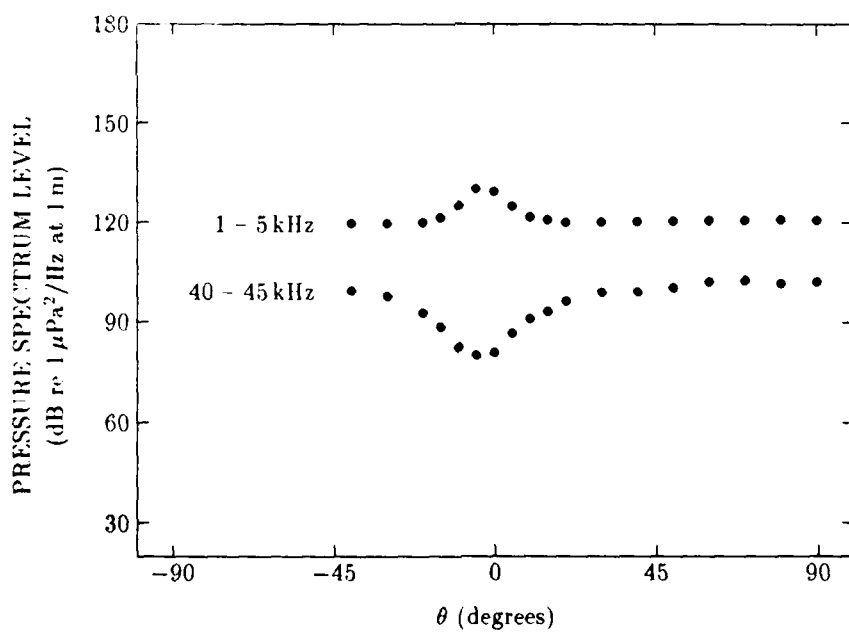


Figure 18: Directivity of Propeller TV1 at 2500 rpm

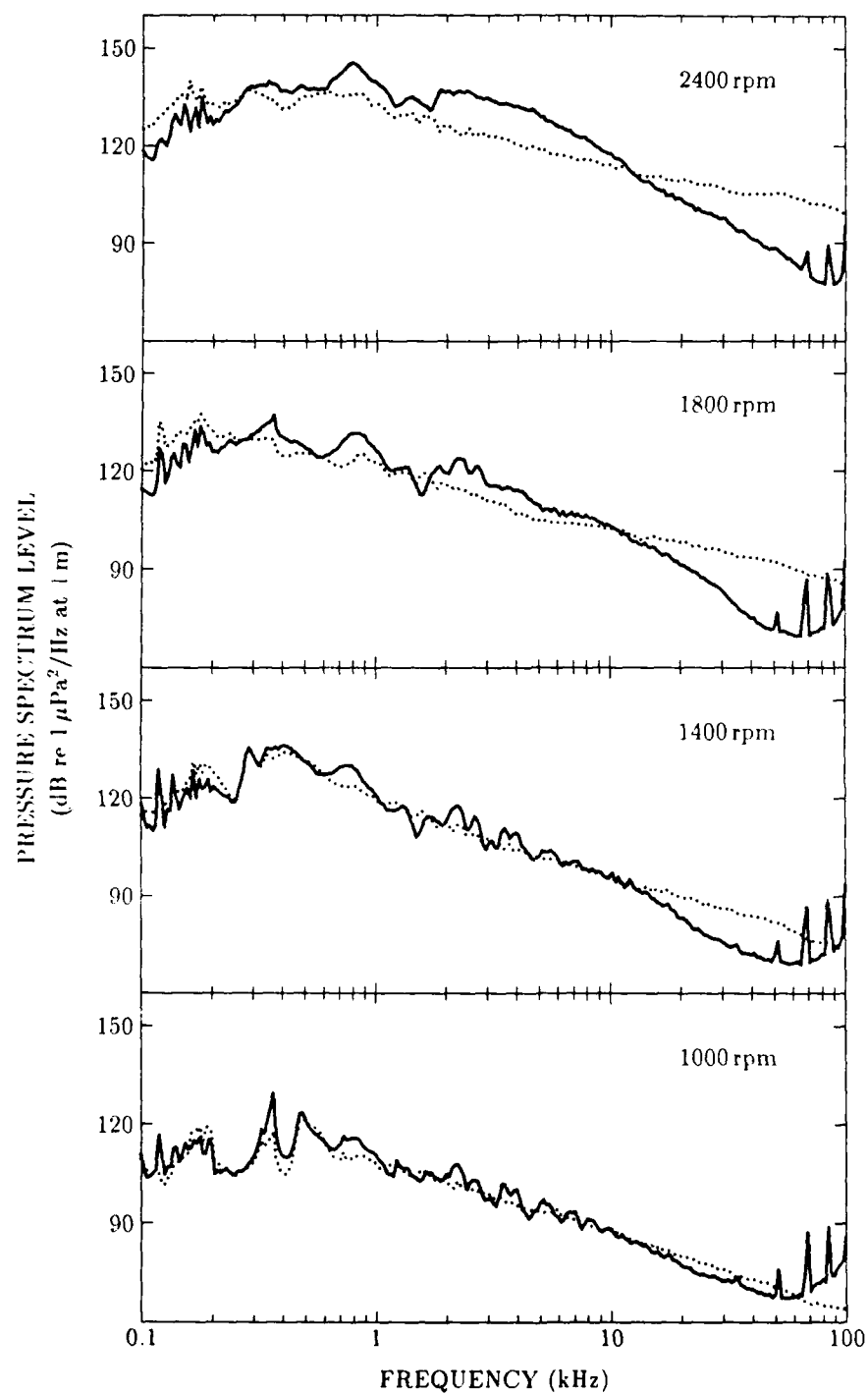


Figure 19: Comparison of spectra measured with Hydrophones 1 (dotted lines) and 3 (solid lines), for Propeller BB, at various rotation rates

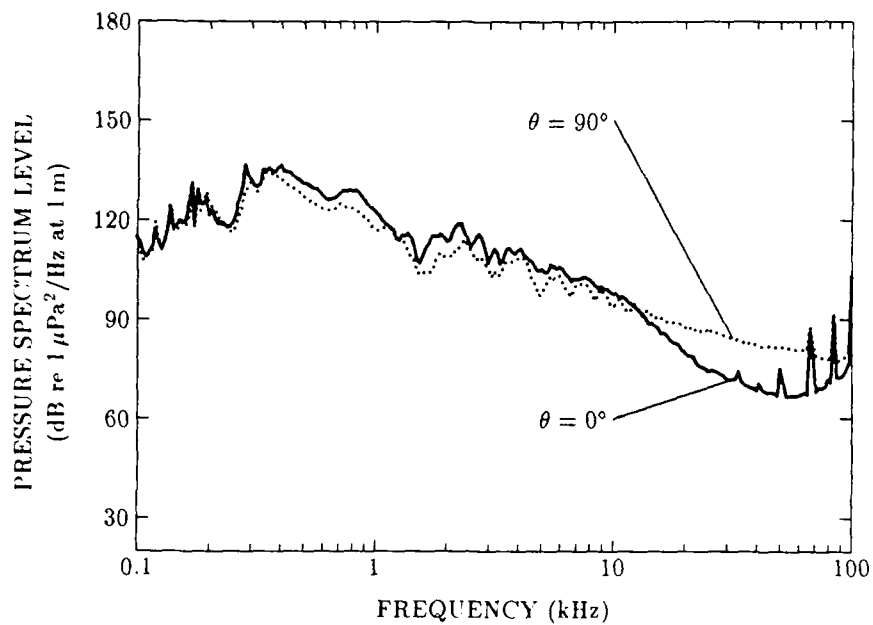


Figure 20: Comparison of spectra at $\theta = 0^\circ$ and 90° for Propeller BB at 1400 rpm

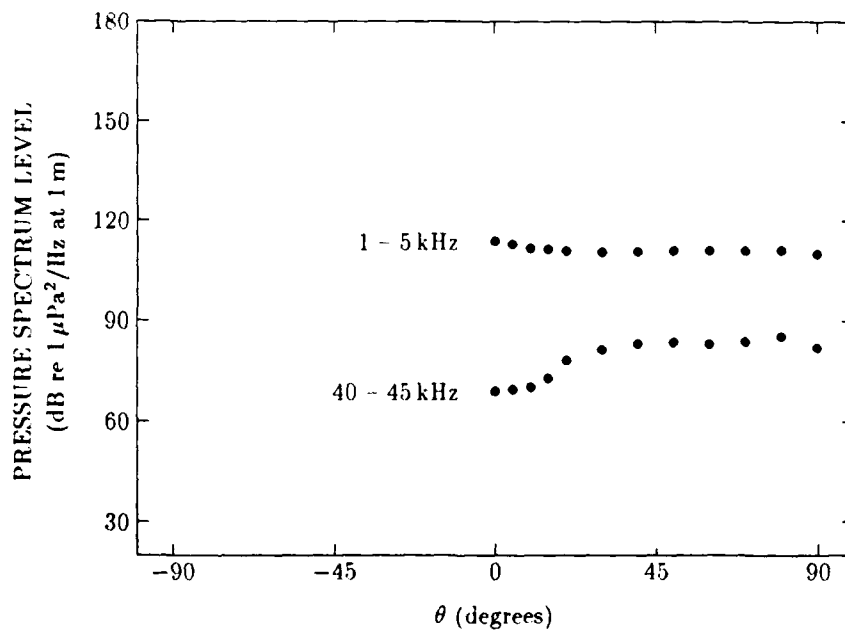


Figure 21: Directivity of Propeller BB at 1400 rpm

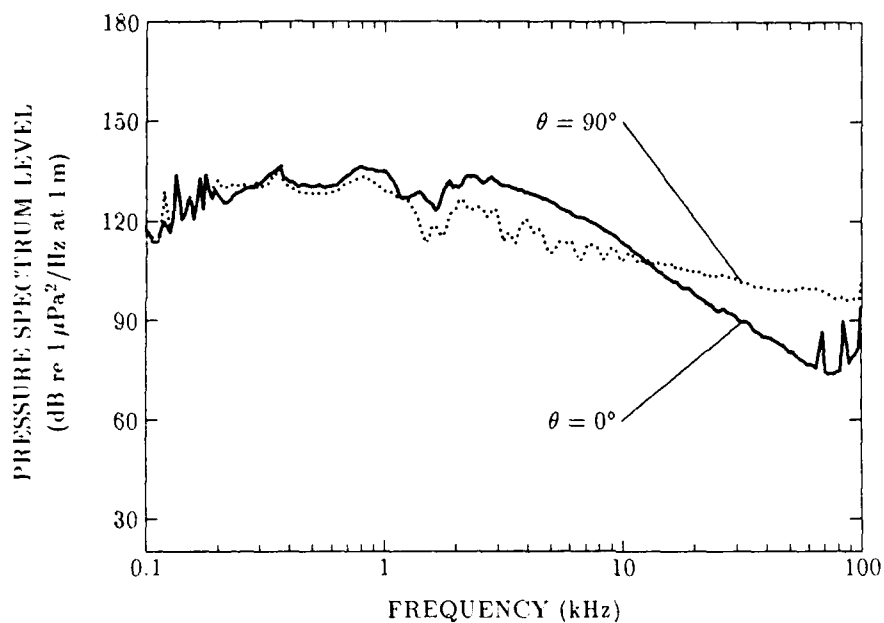


Figure 22: Comparison of spectra at $\theta = 0^\circ$ and 90° for Propeller BB at 2000 rpm

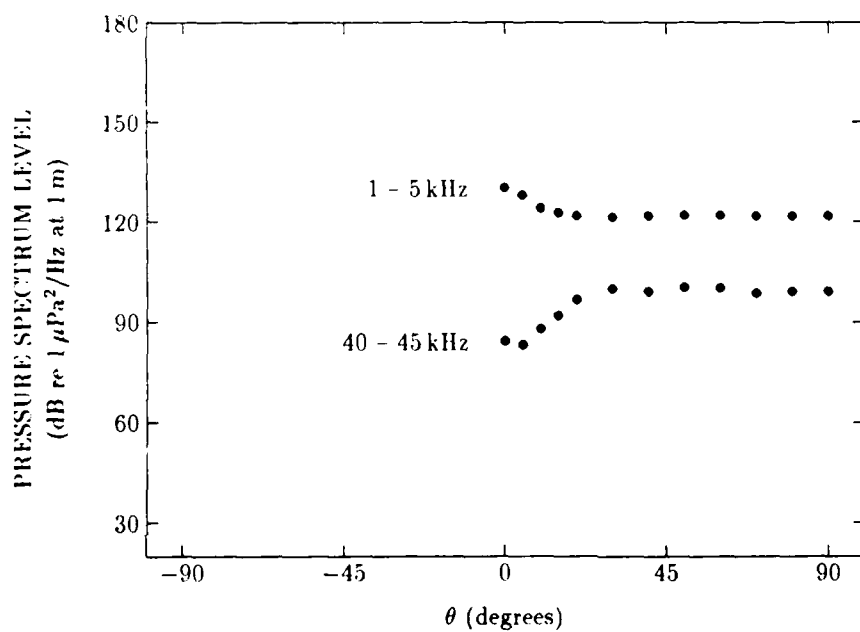


Figure 23: Directivity of Propeller BB at 2000 rpm

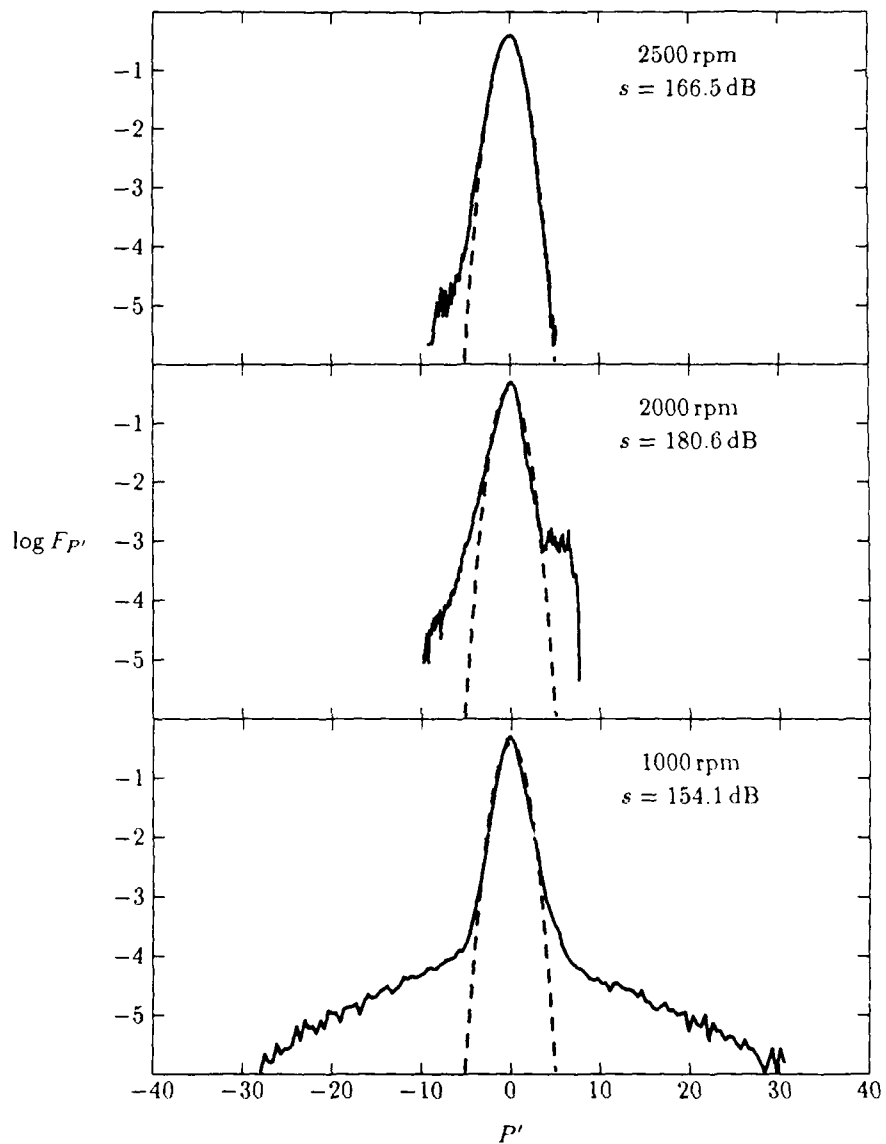


Figure 24: Normalized probability densities for Propeller TV1. For comparison, $\log N_{P'}$ also is shown as the dashed curves.

References

- [1] J. L. Kennedy, N. C. Sponagle, D. W. Wheaton, P. MacDonald, and R. W. Creaser. Video systems for propeller viewing. In *Proceedings of the 22nd American Towing Tank Conference*, 1989.
- [2] J. C. Mallinson. *The Foundations of Magnetic Recording*. Academic Press, 1987.
- [3] J. S. Bendat and A. G. Piersol. *Random Data: Analysis and Measurement Procedures*. John Wiley and Sons, second edition, 1986.
- [4] L. J. Leggat and N. C. Sponagle. The study of propeller cavitation noise using cross-correlation methods. *Journal of Fluids Engineering*, 107:127-133, March 1985.
- [5] N. C. Sponagle and L. J. Leggat. The spacial distribution of acoustic sources at propeller vortex cavitation inception. In *Proceedings of the International Symposium on Cavitation Inception*, pages 191-198, 1984.
- [6] Lord Kelvin. *Mathematical and Physical Papers*, volume IV. Cambridge University Press, 1910.
- [7] J. E. Ffowcs Williams and S. O'Shea. Sound generation by hydrodynamic sources near a cavitated line vortex. *Journal of Fluid Mechanics*, 43:675-688, 1970.
- [8] V. P. Morozov. Theoretical analysis of the acoustic emission from cavitation line vortices. *Soviet Physics - Acoustics*, 19:468-471, 1974.
- [9] J. V. Pylkkänen. Viscous effects on the stability of cavitating line vortices. In *Proceedings of the 14th Symposium on Naval Hydrodynamics*, pages 195-214, 1982.
- [10] P. Ligneul. Theory of tip vortex cavitation noise of a screw propeller operating in a wake. In *Proceedings of the 17th Symposium on Naval Hydrodynamics*, 1988.
- [11] L. D. Landau and E. M. Lifshitz. *Fluid Mechanics*. Pergamon Press, 1959.

UNCLASSIFIED

SECURITY CLASSIFICATION OF FORM
(highest classification of Title, Abstract, Keywords)

DOCUMENT CONTROL DATA		
(Security classification of title, body of abstract and indexing annotation must be entered when the overall document is classified)		
1. ORIGINATOR (the name and address of the organization preparing the document. Organizations for whom the document was prepared, e.g. Establishment sponsoring a contractor's report, or tasking agency, are entered in section 8.) Defence Research Establishment Atlantic P.O. Box 1012, Dartmouth, Nova Scotia B2Y 3Z7	2. SECURITY CLASSIFICATION (overall security classification of the document including special warning terms if applicable) <p style="text-align: center;">UNCLASSIFIED</p>	
3. TITLE (the complete document title as indicated on the title page. Its classification should be indicated by the appropriate abbreviation (S, C, R or U) in parentheses after the title.) <p style="text-align: center;">Noise from Tip Vortex and Bubble Cavitation</p>		
4. AUTHORS (Last name, first name, middle initial. If military, show rank, e.g. Doe, Maj. John E.) <p style="text-align: center;">Sponagle, Neil C.</p>		
5. DATE OF PUBLICATION (month and year of publication of document) <p style="text-align: center;">March 1990</p>	6a. NO. OF PAGES (total containing information. Include Annexes, Appendices, etc.) <p style="text-align: center;">39</p>	6b. NO. OF REFS (total cited in document) <p style="text-align: center;">11</p>
6. DESCRIPTIVE NOTES (the category of the document, e.g. technical report, technical note or memorandum. If appropriate, enter the type of report, e.g. interim, progress, summary, annual or final. Give the inclusive dates when a specific reporting period is covered.) <p style="text-align: center;">DREA Technical Memorandum</p>		
8. SPONSORING ACTIVITY (the name of the department project office or laboratory sponsoring the research and development. Include the address.) 		
9a. PROJECT OR GRANT NO. (if appropriate, the applicable research and development project or grant number under which the document was written. Please specify whether project or grant.) <p style="text-align: center;">1AF</p>	9b. CONTRACT NO. (if appropriate, the applicable number under which the document was written) 	
10a. ORIGINATOR'S DOCUMENT NUMBER (the official document number by which the document is identified by the originating activity. This number must be unique to this document.) <p style="text-align: center;">DREA Technical Memorandum 90/202</p>	10b. OTHER DOCUMENT NOS. (any other numbers which may be assigned this document either by the originator or by the sponsor) 	
11. DOCUMENT AVAILABILITY (any limitations on further dissemination of the document, other than those imposed by security classification) <div style="margin-left: 20px;"> <input checked="" type="checkbox"/> (X) Unlimited distribution <input type="checkbox"/> () Distribution limited to defence departments and defence contractors; further distribution only as approved <input type="checkbox"/> () Distribution limited to defence departments and Canadian defence contractors; further distribution only as approved <input type="checkbox"/> () Distribution limited to government departments and agencies; further distribution only as approved <input type="checkbox"/> () Distribution limited to defence departments; further distribution only as approved <input type="checkbox"/> () Other (please specify): </div>		
12. DOCUMENT ANNOUNCEMENT (any limitations to the bibliographic announcement of this document. This will normally correspond to the Document Availability (11). However, where further distribution (beyond the audience specified in 11) is possible, a wider announcement audience may be selected.) 		

UNCLASSIFIED

SECURITY CLASSIFICATION OF FORM

DCD03 2-00 87

UNCLASSIFIED
SECURITY CLASSIFICATION OF FORM

13. **ABSTRACT** (a brief and factual summary of the document. It may also appear elsewhere in the body of the document itself. It is highly desirable that the abstract of classified documents be unclassified. Each paragraph of the abstract shall begin with an indication of the security classification of the information in the paragraph (unless the document itself is unclassified) represented as (S), (C), (R), or (U). It is not necessary to include here abstracts in both official languages unless the text is bilingual).

✓ This paper presents results from experiments designed to study the sound from different types of propeller cavitation. The propellers used in the tests produced tip vortex and travelling bubble cavitation. The spectral content, directivity, and waveform of the far-field sound were measured, in essentially free-field conditions up to 100 kHz. These data were then correlated with information about the cavity dynamics, obtained from visual observations. Vibrational modes on the tip vortex cavities produced sound at characteristic frequencies. Bubble cavitation by itself produced very broadband noise, and strongly affected the vortex cavitation noise mechanisms if the free bubbles entered the tip vortices. The noise from both kinds of cavitation was directional. *Revised*

14. **KEYWORDS, DESCRIPTORS or IDENTIFIERS** (technically meaningful terms or short phrases that characterize a document and could be helpful in cataloguing the document. They should be selected so that no security classification is required. Identifiers, such as equipment model designation, trade name, military project code name, geographic location may also be included. If possible keywords should be selected from a published thesaurus e.g. Thesaurus of Engineering and Scientific Terms (TEST) and that thesaurus-identified. If it not possible to select indexing terms which are Unclassified, the classification of each should be indicated as with the title)

✓ Propeller
Cavitation
Noise,
Spectra
Directivity
Waveform
Revised

UNCLASSIFIED
SECURITY CLASSIFICATION OF FORM